

## 3-D seismic attenuation structure of Long Valley caldera: looking for melt bodies in the shallow crust

Janire Prudencio<sup>1,2</sup> and Michael Manga<sup>3,4</sup>

<sup>1</sup>*Department of Theoretical physics and Cosmos, Physics of the Earth area, University of Granada, Profesor Clavera 12, 18071 Granada, Spain.*

*E-mail: janire@ugr.es*

<sup>2</sup>*Instituto Andaluz de Geofísica, University of Granada, Campus de Cartuja, Granada, Spain*

<sup>3</sup>*Department of Earth and Planetary Science, University of California at Berkeley, 307 McCone Hall, Berkeley, CA 94720, USA*

<sup>4</sup>*Berkeley Seismological Laboratory, University of California-Berkeley, 215 McCone Hall, Berkeley, CA 94720, USA*

Accepted 2019 November 29. Received 2019 November 27; in original form 2019 October 11

### SUMMARY

Unrest at Long Valley caldera (California) during the past few decades has been attributed to the ascent of hydrothermal fluids or magma recharge. The difference is critical for assessing volcanic hazard. To better constrain subsurface structures in the upper crust and to help distinguish between these two competing hypotheses for the origin of unrest, we model the 3-D seismic attenuation structure because attenuation is particularly sensitive to the presence of melt. We analyse more than 47 000 vertical component waveforms recorded from January 2000 through November 2016 obtained from the Northern California Earthquake Data Center. We then inverted the *S*-to-coda energy ratios using the coda normalization method and obtained an average *Q* of 250. Low attenuation anomalies are imaged in the fluid-rich western and eastern areas of the caldera, one of which corresponds to the location of an earthquake swarm that occurred in 2014. From a comparison with other geophysical images (magnetotellurics, seismic tomography) we attribute the high attenuation anomalies to hydrothermal systems. Average to high attenuation values are also observed at Mammoth Mountain (southwest of the caldera), and may also have a hydrothermal origin. A large high attenuation anomaly within the caldera extends from the surface to the depths we can resolve at 9 km. Shallow rocks here are cold and this is where earthquakes occur. Together, these observations imply that the high attenuation region is not imaging a large magma body at shallow depths nor do we image any isolated high attenuation bodies in the upper  $\approx 8$  km that would be clear-cut evidence for partially molten bodies such as sills or other magma bodies.

**Key words:** Hydrothermal systems; Seismic Attenuation; Caldera.

### 1 INTRODUCTION

An improved interpretation of unrest at volcanoes requires that we identify the presence of, and changes in, the location, geometry and size of possible magma bodies and pathways (Cashman & Giordano 2014). Joint interpretation of different geophysical parameters is one of the best approaches to characterize subsurface structures because different measurements have different sensitivities to physical and geometric properties of magma bodies. Seismic attenuation can be particularly sensitive to the presence of melt. Seismic attenuation models of volcanic systems thus complement other geophysical images such as those obtained from seismic tomography, deformation or resistivity. At Campi Flegrei caldera, Italy, for example, seismic attenuation models (De Siena *et al.* 2017a, b) have been used to infer that earthquake swarms along with uplift and subsidence (e.g. Chiodini *et al.* 2016, 2017) are produced by the migration and accumulation of hot fluids.

Long Valley caldera (Fig. 1), an ellipsoidal caldera located in eastern California, hosted eruptions both inside and outside the structural caldera. Recent unrest at Long Valley caldera began in 1978 with the uplift ( $\approx 83$  cm, Montgomery-Brown *et al.* 2015) of the resurgent dome (Rundle & Hill 1988), four  $M \approx 6$  earthquakes in 1980 (Taylor & Bryant 1980) and numerous earthquake swarms including a major swarm in 1983 and a large, extended-duration swarm in 1997–1998 (Prejean *et al.* 2002; Hill *et al.* 2003). The most recent earthquake swarm was reported in 2014 (Shelly *et al.* 2015a). It was the largest swarm in the caldera since the 1997–1998 swarm and was located beneath the southeast edge of the resurgent dome. All of these swarms were accompanied by rapid uplift of the central resurgent dome (e.g. the 1997–1998 swarm was accompanied by more than 20 cm of uplift) and no significant subsidence has been documented (Langbein 2003; Hill 2006; Montgomery-Brown *et al.* 2015). A key question is whether the unrest has a hydrothermal origin or results from magma intrusion.

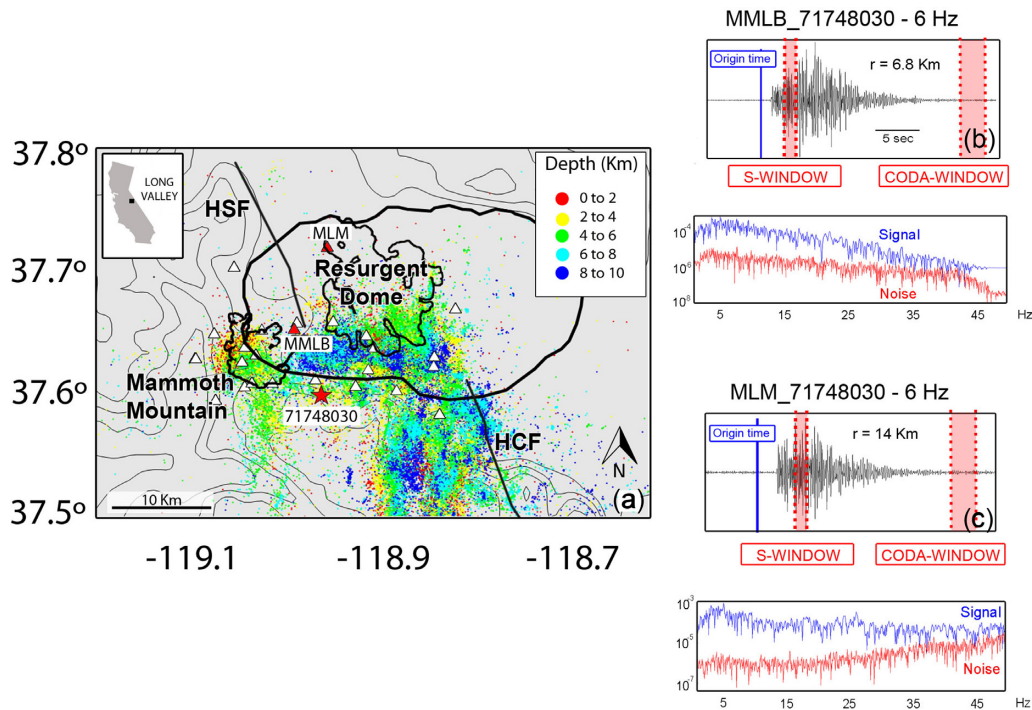


**Figure 1.** (a) Topographic map of Long Valley Caldera. The erosional rim of the caldera is marked with a thick black line. Earthquakes used in the analysis are also shown as coloured circles, each corresponding to different depths. White triangles are the stations used in the analysis (25 stations). The red star with its label (71748030) and two red triangles labelled MLM and MMLB correspond to the earthquake and two stations, respectively, of the waveform examples on the right. The box in the inset map shows the location of Long Valley Caldera in California. (b) Vertical record of earthquake 71748030 recorded at station MMLB. S window and coda window lengths used in the analysis are represented with red colour. Below, Signal spectrum is plotted with blue colour and obtained by analysing 1-s time window after  $P$ -wave arrival time and noise spectrum is plotted with a red line, and it corresponds to 1-s time window 5 s before  $P$ -wave arrival time. (c) Same as b but for MLM station. HSF, Hartely Spring Fault; HCF, Hilton Creek Fault.

Geological and geophysical studies at Long Valley highlight the challenge in unambiguously relating ongoing unrest to subsurface magma bodies. A variety of geophysical studies suggest that melt is present today. A host of seismic images have been produced over the past three decades (e.g. Dawson *et al.* 1990; Romero Jr. *et al.* 1993; Weiland *et al.* 1995; Foulger *et al.* 2003; Seccia *et al.* 2011; Lin 2015; Flinders *et al.* 2018; Schmandt *et al.* 2019). These generally infer the presence of melt in the mid to lower crust. Flinders *et al.* (2018), for example, identify low velocity anomalies that can be explained by (possibly very large volumes of) partial melt. Radial seismic anisotropy and low velocities also favor the presence of melt at depths of  $\approx 5$ –18 km (Jiang *et al.* 2018). Seismic reflections from a depth of  $\approx 8$  km may also be mapping the top of a magma reservoir (Nakata & Shelly 2018). Magnetotelluric images do not identify resistivity anomalies at more shallow depths that could be attributed to partial melt (Peacock *et al.* 2016). To quote Flinders *et al.* (2018), however, ‘we cannot discriminate between magmatic intrusion and mobilization of exsolved fluids as the driver of recent uplift at Long Valley, but we can conclude the mid-crustal reservoir is still melt-rich’. Models for inflation based on microgravity and geodetic data add the dimension of time and can connect uplift to the source of deformation and, hence, anomalies in geophysical images. Because the inferred depth of deformation sources is similar to depths at which magma might exist or accumulate, several geodetic studies have attributed the uplift to magma intrusion (e.g. Battaglia *et al.* 2003a, b; Langbein 2003; Newman *et al.* 2006; Feng & Newman 2009; Montgomery-Brown *et al.* 2015).

The geological record reviewed by Hildreth (2017), in contrast, shows that the most recent volcanic activity has been outside the

caldera along a north–south trending zone that includes Mammoth Mountain (200–500 ka), Mono-Inyo craters (35–0.6 ka) and Mono Lake (250 years old). Thus, based on the geophysical and geological data, two very different processes have been invoked to explain the inflation of the resurgent dome: magmatic injection (e.g. Smith & Bailey 1968; Battaglia *et al.* 2003b; Langbein 2003; Montgomery-Brown *et al.* 2015) or ascending low-viscosity aqueous fluids (e.g. Hurwitz *et al.* 2007; Hutnak *et al.* 2009; Hildreth 2017).

The goal of this study is to create a 3-D model of seismic attenuation beneath Long Valley caldera to search for anomalies that could be attributed to either magmatic or hydrothermal systems within the upper  $\approx 10$  km of the crust. As the images are snapshots of Earth properties, we are not able to address temporal changes. We can, however, search for spatial anomalies that could be the magmatic or hydrothermal sources of deformation.

## 2 DATA AND METHOD

### 2.1 Coda normalization method

The coda normalization (CN) method measures the ratio between direct- and coda-waves energy in a given time interval:

$$\ln \left( \frac{A_{ij}^D(f_c)}{A_{ij}^C(f_c, t_c)} \cdot r_{ij} \right) = K(f_c, t_c) - \pi f \int_{r_{ij}} \frac{dl}{v(l)Q(l)}, \quad (1)$$

where  $Q^{-1}$  is the attenuation,  $A_{ij}^D$  and  $A_{ij}^C$  are the energies of  $S$  and coda expressed as spectral amplitudes,  $r_{ij}$  is the total length of the  $ij$ th ray,  $K(f_c, t_c)$  is a constant for each frequency depending

on the average properties of the medium,  $v(l)$  is the velocity of the medium measured along the ray path,  $f_c$  corresponds to the central frequency and  $t_c$  is the lapse-time. More details on the application of CN method can be found in Del Pezzo *et al.* (2006). The CN method (Del Pezzo *et al.* 2006) is based on the phenomenological properties of the coda as expressed by Aki (1980), who calculated the coda energy as a function of the average medium properties. The CN method assumes the validity of the single scattering model for simplicity and that radiation pattern effects are strongly reduced (see the demonstration by Del Pezzo *et al.* 2006) and broadly applied in both tectonic and volcanic regions (e.g. Bianco *et al.* 1999, 2005; Tuvé *et al.* 2006; Badi *et al.* 2009). The inversion scheme calculates the attenuation factor averaged over the whole volume under study and the corresponding geometrical spreading. These parameters are obtained by a simple least square approach assuming an average velocity. It is possible to study the potential influence of single path coda- $Q$  value using each source–station pair. However, it is well-known that coda- $Q$  values are only reliable when they average thousands of pair estimations. In a second step, model parameters are obtained as variations of the inverse quality factors with the average quality factor in the blocks of the defined grid. Hence, keeping the geometrical spreading constant, it is assumed that the quality factors are a measurement of both intrinsic and scattering effects. It is thus worthwhile to compare total- $Q$  values with the 2-D attenuation maps obtained previously by Prudencio *et al.* (2018).

## 2.2 Velocity model and ray tracing

The CN method calculates the inverse total quality factors along the source–station ray path and, hence, to estimate those ray paths, a 3-D seismic velocity model is needed. For the present inversion, we use the velocity model obtained by Lin (2015) to trace rays derived from the seismic velocity tomography of the region using the same data set. Lin (2015) used a data set consisting of 181 809 local earthquakes recorded between 1984 and 2014 by the Northern California Earthquake Data Center (NCEDC 2014). The final inverted data set consisted of 52 230  $P$  and 15 737  $S$  picks.  $P$ - and  $S$ -wave traveltimes were inverted using the simul2000 algorithm (Thurber 1983). The velocity model has a set of nodes whose distance depends on ray density and covers a surface area of  $60 \times 60 \text{ km}^2$ . The node spacing is set at 2 km in horizontal and vertical directions, and a continuous velocity distribution, required for the ray tracing, is calculated by linear interpolation. We applied the Thurber-modified ray-bending approach, as implemented by De Siena *et al.* (2010) to the 3-D velocity model from Lin (2015). This method has been successfully applied in strong velocity contrast regions like volcanoes. From the surface to a 10 km depth, the ray density (Fig. 2) confirms the applicability of attenuation tomography between these depths (depths reported relative to sea level). Although our earthquake data set comprises data from the surface to a 10 km depth, we do not interpret below 9 km depth, as the Lin (2015) model is well resolved from surface to 4 km (b.s.l.) for the whole area and to 9 km (b.s.l.) for the southern part of the caldera.

## 2.3 S-wave attenuation tomography

We analysed vertical-component seismic recordings of 3694 local earthquakes ( $M \geq 1.5$ ) from the beginning of January 2000 through the end of November 2016 obtained from the Northern California Earthquake Data Center (NCEDC 2014) and with focal depths shallower than 10 km. The first data set included a total of 73 sites

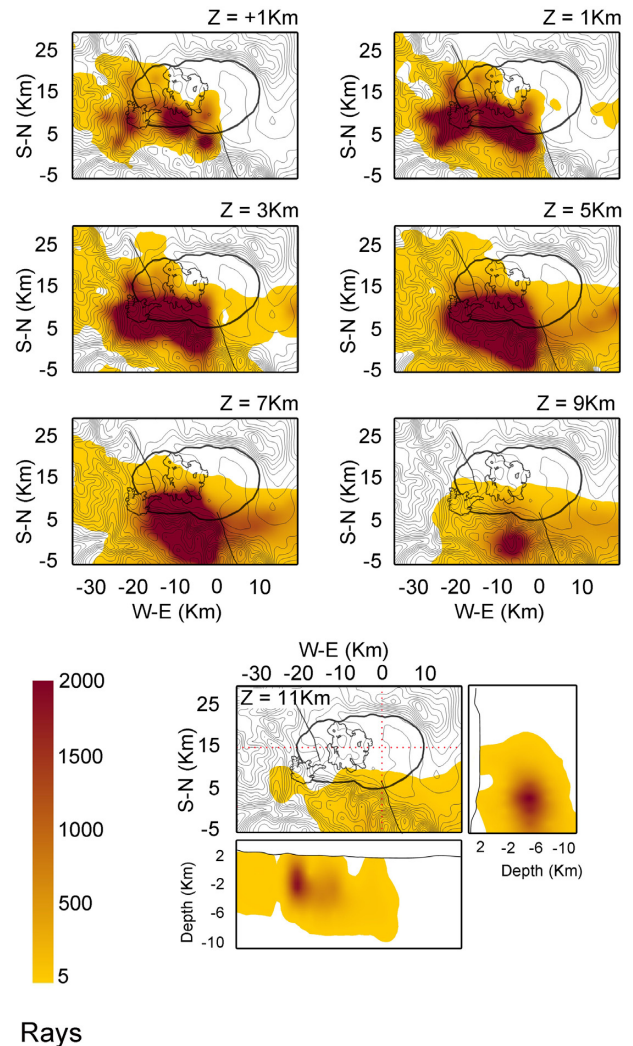


**Figure 2.** Surface projection of ray density for Long Valley caldera. The highest density grids are crossed by  $\geq 1500$  seismic rays. Lower-density cells are crossed by  $\geq 5$  seismic rays. White areas are those with less than five rays (or no rays). The colour bar used in the map views is the same as for depth sections. Contour lines at 100 m intervals show the land surface elevation.

with short-period geophones and broadband sensors which were corrected for instrument responses and a 0.5 Hz high-pass filter was applied to minimize microseism noise. In this study we used the data set used to obtain 2-D intrinsic and scattering attenuation structure by Prudencio *et al.* (2018) consisting of 8628 waveforms registered at 25 stations (Fig. 1a). The data set obtained by Prudencio *et al.* (2018) contain all the waveforms with signal-to-noise higher than 2 at 6 Hz (central frequency), and the rest were rejected. We plot two vertical records produced by an earthquake located in the SSW of the caldera at a depth of 2.5 km (event 71748030 occurred on 2012/03/15 04:55:54.35) and registered by stations MLM and MMLB (Figs 1b and c) with all processing as described. We inverted the  $S$ -to-coda energy ratios using the MURAT code in a single-step inversion (De Siena *et al.* 2014a). The estimation of uncertainties, smoothing parameter and a stability test can be found in Appendix A. We set the start time of the coda window at 15 s after the  $S$ -wave arrival. We use 1.5 and 3 s windows for  $S$  and coda windows (Figs 1b and c). We obtained an average  $Q$  of 250 by the inversion of energy ratios. According to resolution tests in Appendix B (Figs B1 and B2), the optimum size of the node spacing

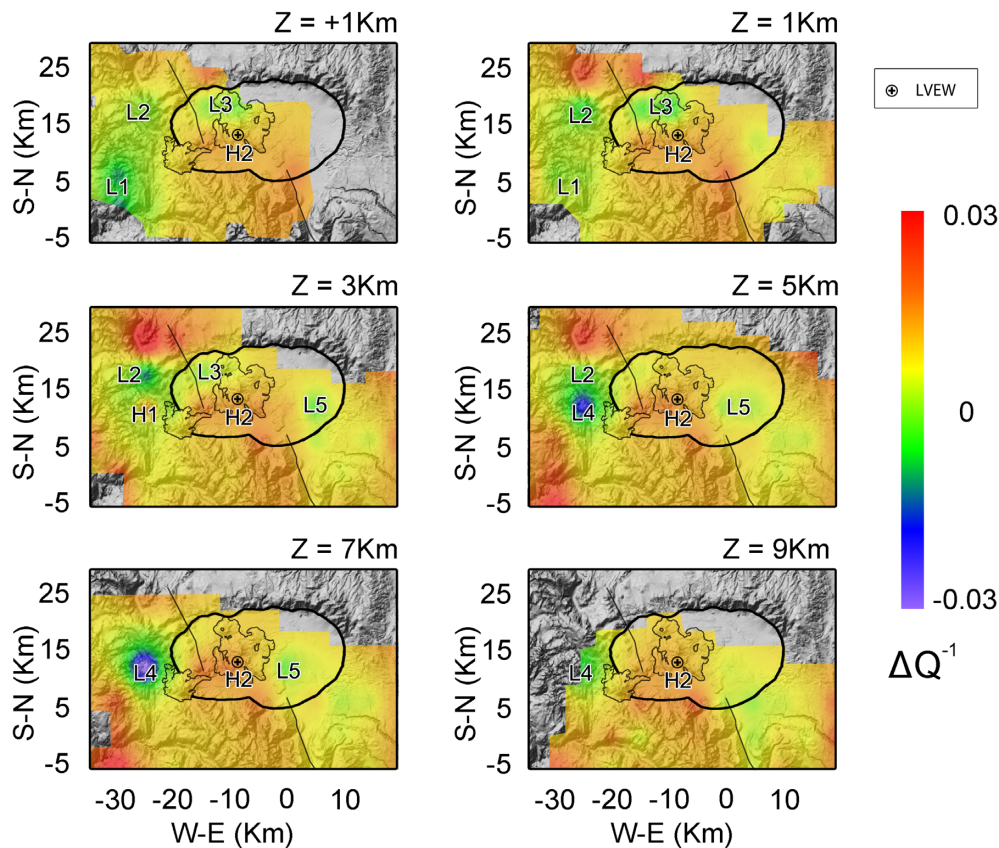


**Figure 3.** Six horizontal sections through the attenuation tomography model. The colour scale shows the variations of the attenuation model with respect to the average quality factor. The high and low attenuation anomalies discussed in the text are shown.

for inversion is  $4.5 \times 4.5 \times 2$  km. Figs 3 and 4 show the variations with respect to the inverse of the average quality factor in the 3-D space ( $\Delta Q^{-1}$  in per cent).

### 3 RESULTS AND DISCUSSIONS

Explaining the relationship between seismic attenuation values and rock properties is still a complex and often ambiguous task. Low velocity and high attenuation do not always mean the presence of melt beneath volcanoes: fluids, gases, faults and more generally, unconsolidated and heavily fractured materials can also produce high attenuation (and low velocity). With the goal of reaching the most realistic model, we interpret our images together with other geophysical studies such as velocity and conductivity models, as well as 2-D attenuation maps obtained by Prudencio *et al.* (2018).

#### 3.1 $Q$ values in Long Valley

The inversion of energy ratios provides an average  $Q$  of 250 for Long Valley caldera. As observed in other volcanic regions (e.g. De Siena *et al.* 2014b; Prudencio *et al.* 2015b) this value is lower than the mean value estimated for Earth's crust (Sato *et al.* 2012). The average total- $Q$ , however, is higher than at other volcanic regions, such as Tenerife ( $Q = 125$ , Prudencio *et al.* 2015b), Mt Etna ( $Q = 75$ , Martínez-Arevalo *et al.* 2005) and Deception island ( $Q = 29$ , Prudencio *et al.* 2015a). A possible explanation for this

difference could be the influence of the crystalline basement rocks, which are characterized by very high  $Q$  values.

In Fig. 3 we plot six horizontal slices obtained from 1 km above sea level to an 11 km depth and in Fig. 4 we include eight vertical sections. Fig. 5 is a 3-D view of the main structures identified below the caldera. From Figs 3 and 4 we observe high attenuation at all depths below the resurgent dome. This structure coincides with that imaged by Eberhart-Phillips (2016) using local earthquakes in northern California. She further inferred two different partial melt features below Long Valley caldera at  $\approx 3$  and  $\approx 15$  km depth. The shallowest structure occurs at 1–4 km below the caldera and shows  $Q_s < 100$  at 1 km depth. Prudencio *et al.* (2018) imaged a low-intrinsic and low-scattering attenuation anomaly in the centre-south of the caldera and a high-intrinsic and high-scattering body corresponding to the location of the 2014 earthquake swarm. Although similar, there are limitations to our ability to compare our 3-D attenuation images with previous attenuation studies. The Eberhart-Phillips (2016) models are regional models for northern California and therefore the resolution is not detailed enough to image the structures under Long Valley caldera that we resolve. On the other hand, the Prudencio *et al.* (2018) images have higher spatial resolution but lack vertical resolution as the models are an average over the first 3–5 km below the caldera and average all structures up to those depths.

In the following, we will discuss and describe in detail those anomalies we believe are the most relevant and those that we can

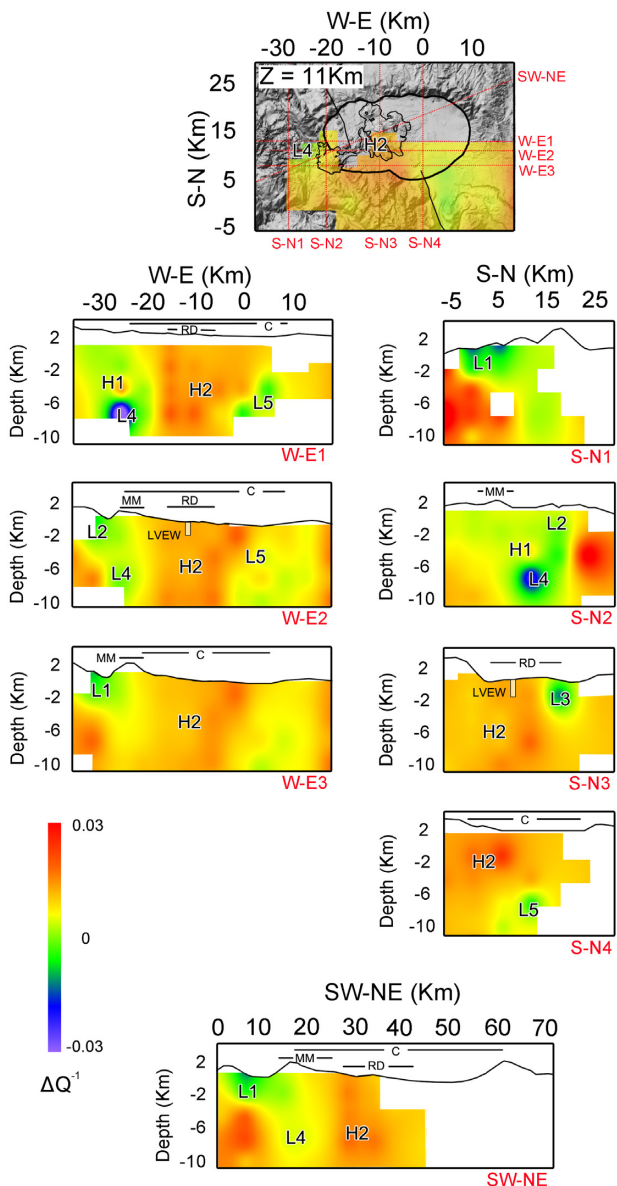


**Figure 4.** Same as Fig 3 but for 8 vertical slices. (C: caldera rim; RD: resurgent dome; MM: Mammoth Mountain).

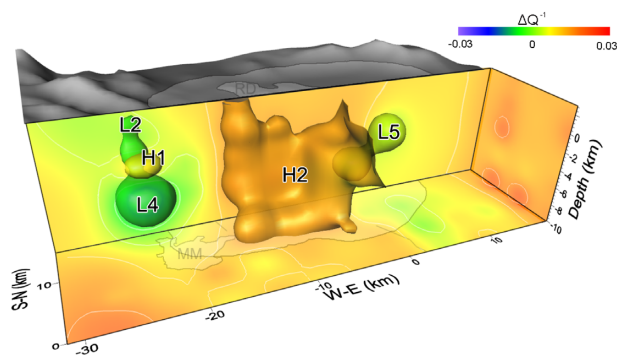


**Figure 5.** 3-D view of the attenuation model showing the best resolved anomalies beneath Long Valley caldera. Isosurface values correspond to: green:  $-0.006$ , light green:  $0.003$ , yellow:  $0.006$  and orange:  $0.013$ .

associate with other geological and geophysical features. These anomalies are identified as L (low) and H (high) in Figs 3–5.

### 3.1.1 Attenuation structure below the resurgent dome

At shallow depths (from +1 to 1 km) there is a low attenuation anomaly below the northern part of the resurgent dome (L3) that extends from 1 km a.s.l. to 3 km b.s.l. The location of the anomaly and its attenuation may be interpreted as a consolidated or cold body and, hence, not related to an active hydrothermal system. This anomaly was also imaged as low attenuation in  $Q_i^{-1}$  and  $Q_s^{-1}$  2-D models (Prudencio *et al.* 2018, an average of first 3–5 km). Lin (2015) found this anomaly as low velocity between 2 km a.s.l. and sea level and as high velocity below sea level and high  $V_p/V_s$  ratio between 2 km a.s.l. and 2 km b.s.l. and lower ratio below ( $<1.68$ ). Peacock *et al.* (2016) identified this body as a low conductivity region and finally, Seccia *et al.* (2011) identified a shallow high velocity anomaly from 1 to 5 km below the surface in the same region. Except for the high  $V_p/V_s$  ratio, all the studies mentioned above, suggest that the anomaly is not related to hot fluids. Sorey *et al.* (1991) and Sackett *et al.* (1999) found a body ascribed to hydrothermal clay and mineral alteration under resurgent dome. It is possible that L3 is hydrothermally altered, where fractures have been filled which decreases attenuation. On the other hand, although the anomaly is recovered in the synthetic anomaly test, it has to be interpreted with some caution as it is located at the edge of the resolved model and there may be artefacts from border effects that compromise the image.

Another medium-low attenuation anomaly can be observed east of the resurgent dome (L5) at deeper depths (3–7 km). As with L3, this anomaly may be interpreted as a consolidated or cold body and, hence, not related to hot fluids. Prudencio *et al.* (2018) also found medium-low  $Q_i$  and very low  $Q_s$  values. In the Lin (2015) model this region appears as high velocity and medium-low  $V_p/V_s$  ratio, which are consistent with cold rocks. Lucic *et al.* (2015) sampled soil gas within Long Valley caldera and attributed the lack of hydrothermal gas signatures in this region to a thick sedimentary and volcanic fill keeping deep fluids from the shallow topographically forced regional flows and may be the reason for the absence of hot fluids. De Siena *et al.* (2017a) correlated a low attenuation body with the location of repeated injection-induced seismicity at Campi Flegrei. At Long Valley the L5 anomaly coincides with the location of 2014 earthquake swarm and the majority of seismic activity (Shelly *et al.* 2015b).

The most interesting anomaly, due to the open question about the location of a (possible) magma body, is the high anomaly located beneath the caldera. We observe a high attenuation anomaly in the centre-south of the caldera, below the southern part of the resurgent dome which extends to the depths resolved in our model (H2). The attenuation behaviour of the region and its extent makes it reasonable to invoke the existence of a large partial melt body (e.g. Flinders *et al.* 2018; Jiang *et al.* 2018). On the other hand, a large hydrothermal system (e.g. Peacock *et al.* 2016; Hildreth 2017) may produce a similar anomaly. Seccia *et al.* (2011) found a  $\approx 4$  km thick layer centred at  $\approx 9$  km depth, interpreted as partial melt. Nakata & Shelly (2018) recognized waves that are reflected at the top of the low-velocity body, which may be residual magma from the caldera-forming eruption. They located the depth of the imaged magmatic system roof around 8.2 km below the surface. High  $V_p/V_s$  is generally a good indicator of fluids or magma and interpreted together

with attenuation images, can help distinguish between hydrothermal or magmatic systems. Lin (2015) found high velocity anomalies from 2 to 6 km and low  $V_p/V_s$  ratio which increases at greater depths in the same region corresponding to suggested partial melt location. Foulger *et al.* (2003) found low  $V_p$  anomalies beneath the southern part of the resurgent dome but not characterized by a high  $V_p/V_s$  ratio, which does not support the interpretation of partial melt emplacement. Attenuation maps obtained by Prudencio *et al.* (2018), which are an average of the first 3–5 km, present average  $Q_i$  values but high  $Q_s$  attenuation (intrinsic attenuation should be high in partially molten rocks). Schmandt *et al.* (2019) summarizing previous imaging studies concluded that the strongest seismic evidence for magma reservoirs beneath Long Valley is found at  $\approx 5$ –15 km depth and it has sharp edges and reduced velocity. Based on these studies, at shallowest depths the anomaly may be related to post-caldera fill (high attenuation and low  $V_p/V_s$  ratio). Unconsolidated deposits and very fractured materials present a high attenuation behaviour as observed in the first kilometre of volcanoclastic deposits at Deception Island by Prudencio *et al.* (2015a). At deeper depths, it is difficult to ascribe this anomaly to only one factor. Moreover, because our model does not extend more than 9 km deep we can not confirm or reject that the anomaly can be related to partial melt placed below 9 km. Given the lack of high intrinsic attenuation or spatially distinct high attenuation anomalies, seismic attenuation images do not identify partially molten bodies in the upper  $\sim 10$  km.

### 3.1.2 Attenuation structure below Mammoth Mountain

The most prominent anomaly at shallowest depths (from +1 to 1 km) is located southwest of Mammoth Mountain, under Iron Mountain (Fig. 1) and is characterized by low attenuation values (L1). This anomaly was also imaged by Prudencio *et al.* (2018) with average-low  $Q_i^{-1}$  and very-low  $Q_s^{-1}$ . Highly consolidated rocks of the Sierran batholith would be the most simple explanation for this anomaly.

At intermediate depths (from 3 to 7 km) the largest anomaly is located west of Mammoth Mountain and it is the lowest attenuation anomaly of the region (L4). Fig. 5 shows that this structure might be linked to a shallower low attenuation anomaly (L2), located to the north. Between L2 and L4, there is a smaller high attenuation anomaly (H1), which is clearly shown in WE vertical section (Fig. 3b, W-E1 and S-N1). It has an extent of 3–4 km (between 2 and 6 km depth). In 2-D attenuation maps presented by Prudencio *et al.* (2018) there is no significant anomaly in the region, as the H1 region is represented by average-high  $Q_i$  and low  $Q_s$  attenuation. This region is characterized by low  $V_p$  and  $V_p/V_s$  at shallower depths and average  $V_p$  and average-high  $V_p/V_s$  at deeper depths (Julian *et al.* 1998; Foulger *et al.* 2003; Lin 2013, 2015; Dawson *et al.* 2016). Peacock *et al.* (2016) imaged a resistive body sandwiched by two conductive bodies between 2 and 6 km depth, corresponding to the location of the 2014 earthquake swarm beneath Mammoth Mountain, however, this anomaly cannot be correlated with our anomaly since H1 is located further west of Mammoth. The presence of small low attenuation bodies embedded in high attenuation active volcanic areas has been observed elsewhere, for example, Mt Etna Volcano (Martínez-Arevalo *et al.* 2005). The common interpretation of the attenuation structure of these paired anomalies is the presence of old or cold magmatic intrusions that condition the ascent paths of younger magma (Díaz-Moreno *et al.* 2018, and references therein). We interpret these high contrast anomalies as the product of older

volcanic structures from Mammoth Mountain and Mono-Inyo eruptions and more recent basalt injections. We are not able to image to the depths with rapidly propagating seismicity that may track dyke intrusions Hotovec-Ellis *et al.* (2018).

Recorded seismic signals and previous tomographic studies have inferred a deeper partial melt body below Mammoth Mountain (Hill 1976; Foulger *et al.* 2003; Hill & Prejean 2005; Peacock *et al.* 2016; Hildreth 2017; Hotovec-Ellis *et al.* 2018). As can be observed from Fig. 4 W-E3 and S-N2 profiles, Mammoth Mountain is characterized by high attenuation between 4 and 10 km depth. Although we find no unambiguous evidence for melt in the form of a very high attenuation body directly below Mammoth Mountain, attenuation images confirm the presence of an attenuating area which may be related to hot rocks or presence of fluids.

## 4 CONCLUSIONS

In this study, we provide a 3-D attenuation model obtained with the coda normalization method. We image a large and continuous high attenuation anomaly below the southcentral part of the caldera and the resurgent dome. We thus see no clear-cut evidence for partially molten bodies or sills in the upper 8 km. Due to limited vertical resolution, we can not reject or confirm the existence of a partial melt body at greater depths.

## ACKNOWLEDGEMENTS

The authors are grateful the thorough and constructive comments and suggestions by Phil Dawson and Jesus Ibañez. Waveform data for this study were accessed through the Northern California Earthquake Data Center (NCEDC), doi:10.7932/NCEDC. JP and MM are supported by the NSF-1521855 Hazard SEES project and JP is partially supported by the Spanish KNOWAVES (TEC2015-68752-R) project. We thank Prof Lin for providing 3-D velocity model. Finally, 3-D attenuation model can be found in Prudencio & Manga (2018), doi:10.6078/D1138N.

## REFERENCES

- Aki, K., 1980. Attenuation of shear-waves in the lithosphere for frequencies from 0.05 to 25 Hz, *Phys. Earth planet. Inter.*, **21**, 50–60.
- Badi, G., Del Pezzo, E., Ibáñez, J.M., Bianco, F., Sabbione, N. & Araujo, M., 2009. Depth dependent seismic scattering attenuation in the Nuevo Cuyo region (southern central Andes), *Geophys. Res. Lett.*, **36**, 24 307–24 310.
- Battaglia, M., Segall, P., Murray, J., Cervelli, P. & Langbein, J., 2003a. The mechanics of unrest at Long Valley Caldera, California: 1. Modeling the geometry of the source using GPS, leveling and two-color EDM data, *J. Volc. Geotherm. Res.*, **127**(3), 195–217.
- Battaglia, M., Segall, P. & Roberts, C., 2003b. The mechanics of unrest at Long Valley Caldera, California.: 2. Constraining the nature of the source using geodetic and micro-gravity data, *J. Volc. Geotherm. Res.*, **127**(3), 219–245.
- Bianco, F., Castellano, M., Del Pezzo, E. & Ibáñez, J.M., 1999. Attenuation of short-period seismic waves at Mt. Vesuvius, Italy, *Geophys. J. Int.*, **138**, 67–76.
- Bianco, F., Del Pezzo, E., Malagnini, L., Di Luccio, F. & Akinci, A., 2005. Separation of depth-dependent intrinsic and scattering attenuation in the northeastern sector of the Italian Peninsula, *Geophys. J. Int.*, **161**(1), 130–142.
- Cashman, K. & Giordano, G., 2014. Calderas and magma reservoirs, *J. Volc. Geotherm. Res.*, **288**, 28–45.
- Chiodini, G., Paonita, A., Aiuppa, A., Costa, A., Caliro, S., De Martino, P., Acocella, V. & Vandemeulebrouck, J., 2016. Magmas near the critical

- degassing pressure drive volcanic unrest towards a critical state, *Nat. Commun.*, **7**, 13712.
- Chiodini, G. *et al.*, 2017. Clues on the origin of post-2000 earthquakes at Campi Flegrei caldera (Italy), *Scient. Rep.*, **7**(1), 4472.
- Dawson, P., Chouet, B. & Pitt, A., 2016. Tomographic image of a seismically active volcano: Mammoth Mountain, California, *J. geophys. Res.*, **121**(1), 114–133.
- Dawson, P.B., Evans, J.R. & Iyer, H.M., 1990. Teleseismic tomography of the compressional wave velocity structure beneath the Long Valley region, California, *J. geophys. Res.*, **95**(B7), 11 021–11 050.
- Del Pezzo, E., Bianco, F., De Siena, L. & Zollo, A., 2006. Small scale shallow attenuation structure at Mt. Vesuvius, *Phys. Earth planet. Inter.*, **157**, 257–268.
- De Siena, L., Amoroso, A., Pezzo, E.D., Wakeford, Z., Castellano, M. & Crescentini, L., 2017a. Space-weighted seismic attenuation mapping of the aseismic source of Campi Flegrei 1983–1984 unrest, *Geophys. Res. Lett.*, **44**(4), 1740–1748.
- De Siena, L., Chiodini, G., Vilardo, G., Del Pezzo, E., Castellano, M., Colombelli, S., Tisato, N. & Ventura, G., 2017b. Source and dynamics of a volcanic caldera unrest: Campi Flegrei, 1983–84, *Scient. Rep.*, **7**(1), 8099.
- De Siena, L., Del Pezzo, E. & Bianco, F., 2010. Seismic attenuation imaging of Campi Flegrei: evidence of gas reservoirs, hydrothermal basins and feeding systems, *J. geophys. Res.*, **115**, doi:10.1029/2009JB006938.
- De Siena, L., Thomas, C. & Aster, R., 2014a. Multi-scale reasonable attenuation tomography analysis (MuRAT): an imaging algorithm designed for volcanic regions, *J. Volc. Geotherm. Res.*, **277**, 22–35.
- De Siena, L., Thomas, C., Waite, G.P., Moran, S.C. & Klemme, S., 2014b. Attenuation and scattering tomography of the deep plumbing system of Mount St. Helens, *J. geophys. Res.*, **118**(11), 8223–8238.
- Díaz-Moreno, A. *et al.*, 2018. New insights on Mt. Etna's crust and relationship with the regional tectonic framework from joint active and passive P-wave seismic tomography, *Surv. Geophys.*, **39**(1), 57–97.
- Eberhart-Phillips, D., 2016. Northern California seismic attenuation: 3D  $Q_p$  and  $Q_s$  models, *Bull. seism. Soc. Am.*, **106** (6), 2558–2573.
- Feng, F. & Newman, A.V., 2009. Constraints on continued episodic inflation at Long Valley Caldera, based on seismic and geodetic observations, *J. geophys. Res.*, **114**(B6).
- Flinders, A., Shelly, D.R., Dawson, P.B., Hill, D.P., Tripoli, B. & Shen, Y., 2018. Seismic evidence for significant melt beneath the Long Valley Caldera, California, USA, *Geology*, **46**(9), 799–802.
- Foulger, G., Julian, B.R., Pitt, A.M., Hill, D.P., Malin, P.E. & Shalev, E., 2003. Three dimensional crustal structure of Long Valley caldera, California, and evidence for the migration of CO<sub>2</sub> under Mammoth Mountain, *J. geophys. Res.*, **108**(3), doi:10.1029/2000JB000041.
- Hildreth, W., 2017. Fluid-driven uplift at Long Valley Caldera, California: geologic perspectives, *J. Volc. Geotherm. Res.*, **341**, 269–286.
- Hill, D.P., 1976. Structure of Long Valley caldera, California, from a seismic refraction experiment, *J. geophys. Res.*, **81**, 745–753.
- Hill, D.P., 2006. Unrest in Long Valley Caldera, California, 1978–2004, *Geol. Soc. Lond. Spec. Publ.*, **269**(1), 1–24.
- Hill, D.P., Langbein, J. & Prejean, S., 2003. Relations between seismicity and deformation during unrest in Long Valley Caldera, California, from 1995 through 1999, *J. Volc. Geotherm. Res.*, **127**(3), 175–193.
- Hill, D.P. & Prejean, S., 2005. Magmatic unrest beneath Mammoth Mountain, California, *J. Volc. Geotherm. Res.*, **146**, 257–283.
- Hotovec-Ellis, A.J., Shelly, D.R., Hill, D.P., Pitt, A.M., Dawson, P.B. & Chouet, B.A., 2018. Deep fluid pathways beneath Mammoth Mountain, California, illuminated by migrating earthquake swarms, *Sci. Adv.*, **4**(8), eaat5258.
- Hurwitz, S., Christiansen, L. & Hsieh, P., 2007. Hydrothermal fluid flow and deformation in large calderas: Inferences from numerical simulations, *J. geophys. Res.*, **112**, doi:10.1029/2006JB004689.
- Hutnak, M., Hurwitz, S., Ingeritsen, S. & Hsieh, P.E., 2009. Numerical models of caldera formation: Effects of multiphase and multicomponent hydrothermal fluid flow, *J. geophys. Res.*, **114**, doi:10.1029/2008JB006151.
- Jiang, C., Schmandt, B., Hansen, S.M., Dougherty, S., Clayton, R.W., Farrel, J. & Lin, F.C., 2018. Rayleigh and S wave tomography constraints on subduction termination and lithospheric foundering in central California, *Earth planet. Sci. Lett.*, **488**, 14–26.
- Julian, B.R., Pitt, A. & Foulger, G., 1998. Seismic image of a CO<sub>2</sub> reservoir beneath a seismically active volcano, *Geophys. J. Int.*, **133**(1), F7–F10.
- Langbein, J., 2003. Deformation of Long Valley Caldera, California: inferences from measurements from 1988 to 2001, *J. Volc. Geotherm. Res.*, **127**(3), 247–267.
- Lin, G., 2013. Seismic investigation of magmatic unrest beneath Mammoth Mountain, California, USA, *Geology*, **41**(8), 847–850.
- Lin, G., 2015. Seismic velocity structure and earthquake relocation for the magmatic system beneath Long Valley Caldera, eastern California, *J. Volc. Geotherm. Res.*, **296**, 19–30.
- Lucic, G., Stix, J. & Wing, B., 2015. Structural controls on the emission of magmatic carbon dioxide gas, Long Valley Caldera, USA, *J. geophys. Res.*, **120**(4), 2262–2278.
- Martínez-Arevalo, C., Patané, D., Rietbrock, A. & Ibáñez, J., 2005. The intrusive process leading to the Mt. Etna 2001 flank eruption: constraints from 3D attenuation tomography, *Geophys. Res. Lett.*, **32**, L21309.
- Montgomery-Brown, E.K., Wicks, C.W., Cervelli, P., Langbein, J., Svarc, J.L., Shelly, D.R., Hill, D.P. & Lisowski, M., 2015. Renewed inflation of Long Valley Caldera, California: 2011–2014, *Geophys. Res. Lett.*, **42**, doi:10.1002/2015GL064338.
- Nakata, N. & Shelly, D.R., 2018. Imaging a crustal low velocity layer using reflected seismic waves from the 2014 earthquake swarm at Long Valley Caldera, California: the magmatic system roof?, *Geophys. Res. Lett.*, **45**(8), 3481–3488.
- NCEDC, 2014. Northern California earthquake data center, UC Berkeley Seismological Laboratory. Dataset.
- Newman, A.V., Dixon, T.H. & Gourmelen, N., 2006. A four-dimensional viscoelastic deformation model for Long Valley Caldera, California, between 1995 and 2000, *J. Volc. Geotherm. Res.*, **150**, 244–269.
- Peacock, J.R., Mangan, M.T., McPhee, D. & Wannamaker, P.E., 2016. Three-dimensional electrical resistivity model of the hydrothermal system in Long Valley Caldera, California, from magnetotellurics, *Geophys. Res. Lett.*, **43**(15), doi:10.1002/2016GL069263.
- Prejean, S., Ellsworth, W.L., Zoback, M. & Waldhauser, F., 2002. Fault structure and kinematics of the Long Valley Caldera region, CA, revealed by high-accuracy earthquake hypocenters and focal mechanism stress inversions, *J. geophys. Res.*, **107**(B12), doi:10.1029/2001JB001168.
- Prudencio, J., De Siena, L., Ibáñez, J.M., Del Pezzo, E., García-Yeguas, A. & Díaz-Moreno, A., 2015a. The 3D attenuation structure of Deception Island (Antarctica), *Surv. Geophys.*, **36**, 371–390.
- Prudencio, J., Ibáñez, J.M., Del Pezzo, E., Martí, J., García-Yeguas, A. & De Siena, L., 2015b. 3D attenuation tomography of the volcanic island of Tenerife (Canary Islands), *Surv. Geophys.*, **36**, 693–716.
- Prudencio, J. & Manga, M., 2018. 3D attenuation model of Long Valley Caldera (CA), UC Berkeley Dash, Dataset, <https://doi.org/10.6078/D1138N>.
- Prudencio, J., Manga, M. & Taira, T., 2018. Subsurface structure at Long Valley caldera imaged with seismic scattering and intrinsic attenuation, *J. geophys. Res.*, **123**(7), 5987–5999.
- Romero, A.E., Jr, McEvilly, T.V., Majer, E.L. & Michelini, A., 1993. Velocity structure of the Long Valley caldera from the inversion of local earthquake P and S travel times, *J. geophys. Res.*, **98**(B11), 19 869–19 879.
- Rundle, J.B. & Hill, D.P., 1988. The geophysics of a restless caldera—Long Valley, California, *Ann. Rev. Earth planet. Sci.*, **16**, 251–271.
- Sackett, P., McConnell, V., Roach, A., Priest, S. & Sass, J., 1999. Long Valley Coring Project, 1998. Preliminary stratigraphy and images of recovered core, US Geological Survey Open-File Report, 99-158.
- Sato, H., Fehler, M.C. & Maeda, T., 2012. *Seismic Wave Propagation and Scattering in the Heterogeneous Earth*, 2nd edn, Springer.
- Schmandt, B., Jiang, C. & Farrel, J., 2019. Seismic perspectives from the western U.S. on magma reservoirs underlying large silicic calderas, *J. Volc. Geotherm. Res.*, **384**, 158–178.
- Seccia, D., Chiarabba, C., DeGori, P. & Hill, D., 2011. Evidence for the contemporary magmatic system beneath Long Valley Caldera from local

- earthquake tomography and receiver function analysis, *J. geophys. Res.*, **116**(B12), doi:10.1029/2011JB008471.
- Shelly, D.R., Ellsworth, W.L. & Hill, D.P., 2015a. Fluid-faulting evolution in high definition: connecting fault structure and frequency-magnitude variations during the 2014 Long Valley Caldera, California, earthquake swarm, *J. geophys. Res.*, **121**(3), doi:10.1002/2015JB012719.
- Shelly, D.R., Taira, T., Prejean, S., Hill, D.P. & Dreger, D.S., 2015b. Fluid-faulting interactions: fracture-mesh and fault-valve behavior in the February 2014 Mammoth Mountain, California, earthquake swarm, *Geophys. Res. Lett.*, **42**, 5803–5812.
- Smith, R.L. & Bailey, R.A., 1968. Resurgent cauldrons, *Geol. Soc. Am.*, **116**, 613–662.
- Sorey, M.L., Suemnicht, G.A., Sturchio, N.C. & Nordquist, G.A., 1991. New evidence on the hydrothermal system in Long Valley caldera, California, from wells, fluid sampling, electrical geophysics, and age determinations of hot-spring deposits, *J. Volc. Geotherm. Res.*, **48**(3–4), 229–263.
- Taylor, G.C. & Bryant, W.A., 1980. Surface rupture associated with Mammoth Lakes earthquakes of 25 and 27 May 1980, in Mammoth Lakes earthquakes of May 1980, Sherburne, R.W.(Editor), Calif. Div. Mines Geol. Sp. Rept. 150, 49-67.
- Thurber, C., 1983. Earthquake locations and three-dimensional crustal structure in the coyote lake area, central california, *J. geophys. Res.*, **88**, 8226–8236.
- Tuvé, T., Bianco, F., Ibáñez, J., Patané, D., Del Pezzo, E. & Bottari, A., 2006. Attenuation study in the Straits of Messina area (southern Italy), *Tectonophysics*, **421**(3–4), 173–185.
- Weiland, C.M., Steck, L.K., Dawson, P.B. & Korneev, V.A., 1995. Non-linear teleseismic tomography at Long Valley Caldera, using three dimensional minimum travel time ray tracing, *J. geophys. Res.*, **100**(B10), 20 379–20 390.

## APPENDIX A: MuRAT CODE: FITTING, PICARD CONDITION AND L-CURVE

The estimate of the average quality factor is obtained by a least square inversion of all data. In Fig. A1 the fit of the decrease of coda normalized energies (cyan circles) with increasing travel time (red dots) is plotted. The black dots correspond to uncertainties of the fitting. It can be observed that uncertainties in our attenuation model are relatively low. The MuRAT code De Siena *et al.* (2014a) provides the Picard condition as a test of stability to compare the singular values with the dot product of the columns of the matrix spanning the data space and the data vector. When the dot products decay to zero more quickly than the singular values, the Picard condition is satisfied. Fig. A2 shows the Picard condition for the inversion of Long Valley data. In our case we can see that the

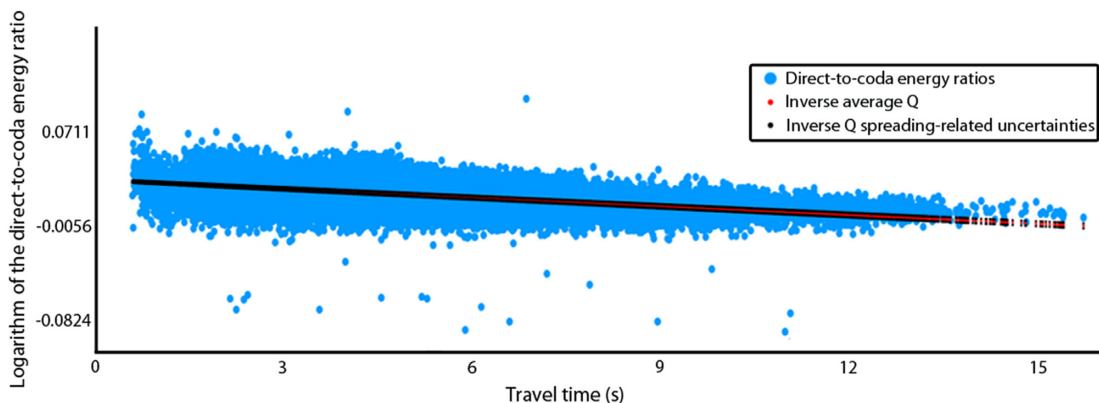


**Figure A1.** Fit of coda normalized energy ratios (cyan circles) with increasing travel time (red dots). The uncertainties of the fit are marked as black dots. Average inverse quality factor  $0.0043836 \pm 4.1971e^{-0.4}$  and geometrical spreading  $0.01809 \pm 0.0151$ .

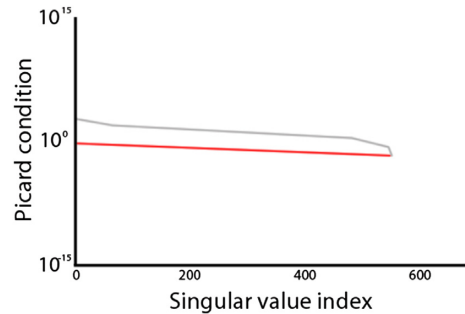


**Figure A2.** Picard condition plot. Dots products are represented as black line and singular values as red line. It can be observed that due to the faster decay of dots products, we should not have instability due to small singular values.

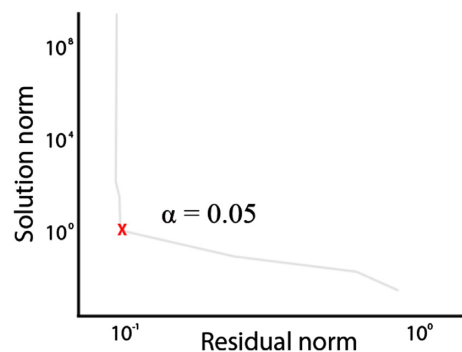


**Figure A3.** L-curve and selected smoothing parameter ( $\alpha$ ) selected for the inversion.

dots products (black line) decay more quickly than singular values (red line), which means that we should not have instabilities due to small singular values. We also obtained the L-curve to estimate the smoothing parameter ( $\alpha$ ) selected using the MuRAT code. In Fig. A3 the obtained L-curve with the MuRAT code is presented. All these plots are obtained with the MuRAT code, a free code working in Matlab R2014b<sup>®</sup>, available at <https://github.com/LucaDeSiena/MuRAT>.

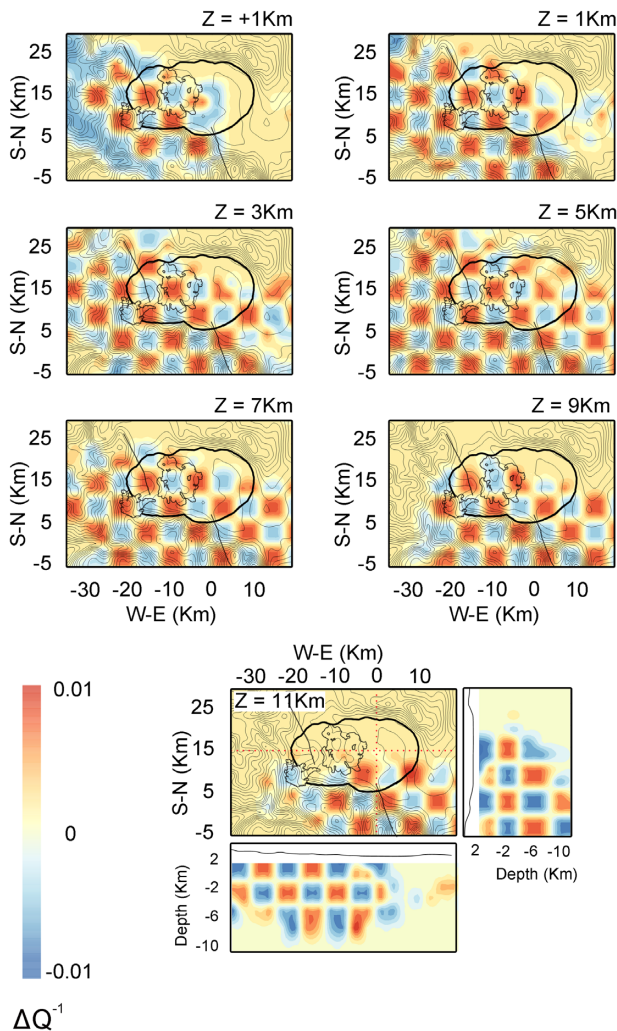


**Figure B1.** Checkerboard tests for Long Valley Caldera. Outputs of the checkerboard test are shown for seven horizontal and two vertical sections. The vertical scale in vertical sections is enlarged for clarity. Contour lines represent the elevation of the area every 100 m.

## APPENDIX B: RESOLUTION TESTS

To check the resolution and stability of the results and robustness of the algorithm, we performed checkerboard and synthetic anomaly tests. The outputs of the checkerboard tests can be observed in Fig. B1. We calculated synthetic  $S$ -to-coda energy ratios and we added Gaussian random error with zero mean and three times the standard deviation.

We calculated synthetic coda energy and added to these values a Gaussian random error with zero mean and three times the standard deviation equal to 20 per cent of the data value. Then, we inverted the synthetic data using the blocks crossed by at least by five rays. The node spacing is 4.5 km in horizontal and 2 km in vertical directions, starting at 2.2 km above sea level, and assigning  $Q$  equal to 100 or 1000. The checkerboard results are well resolved from 1 km a.s.l. to 11 km b.s.l. The checkerboard test results depend on earthquake hypocentre locations and ray coverage. For the case of Long valley caldera, at shallowest depths, better resolution is obtained for the NW region, where most of the stations are located, while for deepest depths the best resolution is obtained in the SW, coinciding with earthquake hypocentre locations. Therefore, those anomalies located close to our resolution limit must be interpreted carefully, as border effect may occur. A spike test to check the effective recovery of the highest and lowest anomalies (including the anomaly at the centre of the caldera) is also performed and shown in Fig. B2. We applied the same procedure as for the checkerboard test. The obtained results show that imposed anomalies (corresponding to anomalies L3, L4, L5 and H2) are well reconstructed with the current data set and ray coverage. The observed displacement of the anomalies is related to the representation method rather the resolution, although those anomalies located in the resolution limit, must be interpreted carefully as for checkerboard test. Both, the checkerboard and synthetic anomalies were created with the MuRAT code.

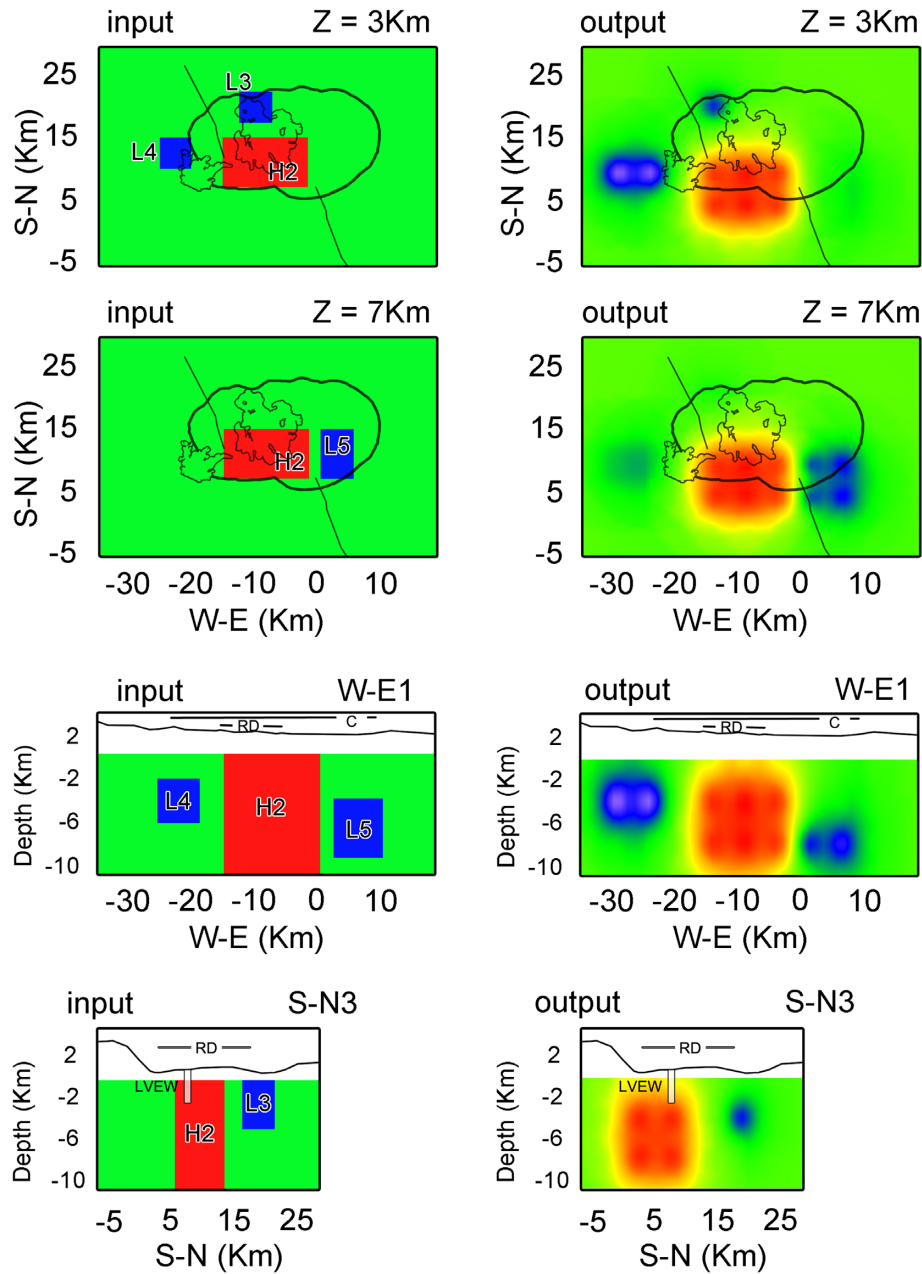


**Figure B2.** Synthetic anomaly tests for Long Valley Caldera. Input (left-hand column) and outputs (right-hand column) of the spike test are shown. We imposed L3, L4 and L5 low attenuation anomalies with  $Q^{-1}$  values equals to  $-0.05$ ,  $-0.08$  and  $-0.05$ , respectively. We also reproduced the high attenuation anomaly at the centre of the caldera (H2) and assigned  $Q^{-1} = 0.06$ . Contour lines represent the elevation of the area every 100 m.